This article has been accepted for inclusion in a future issue of this journal. Content is final as presented, with the exception of pagination.

A Wireless Fiber Photometry System Based on a High-Precision CMOS Biosensor With Embedded Continuous-Time $\Sigma\Delta$ Modulation

Mehdi Noormohammadi Khiarak, *Student Member, IEEE*, Ekaterina Martianova, Cyril Bories, Sylvain Martel, *Fellow, IEEE*, Christophe. D. Proulx, Yves De Koninck, and Benoit Gosselin, *Member, IEEE*

***Abstract*—Fluorescence biophotometry measurements require wide dynamic range (DR) and high-sensitivity laboratory apparatus. Indeed, it is often very challenging to accurately resolve the small fluorescence variations in presence of noise and high-background tissue autofluorescence. There is a great need for smaller detectors combining high linearity, high sensitivity, and high-energy efficiency. This paper presents a new biophotometry sensor merging two individual building blocks, namely a low-noise sensing front-end and a 2nd order continuous-time $\Sigma\Delta$ modulator (CTSDM), into a single module for enabling high-sensitivity and high energy-efficiency photo-sensing. In particular, a differential CMOS photodetector associated with a differential capacitive transimpedance amplifier-based sensing front-end is merged with an incremental 2nd order 1-bit CTSDM to achieve a large DR, low hardware complexity, and high-energy efficiency. The sensor leverages a hardware sharing strategy to simplify the implementation and reduce power consumption. The proposed CMOS biosensor is integrated within a miniature wireless head mountable prototype for enabling biophotometry with a single implantable fiber in the brain of live mice. The proposed biophotometry sensor is implemented in a 0.18-μm CMOS technology, consuming 41 μW from a 1.8-V supply voltage, while achieving a peak dynamic range of 86 dB over a 50-Hz input bandwidth, a sensitivity of 24 mV/nW, and a minimum detectable current of 2.46-$pA_{\rm rms}$ at a 20-kS/s sampling rate.**

***Index Terms*—Capacitive transimpedance amplifier, fiber photometry, fluorescence, high-precision, $\Sigma\Delta$ modulator, optoelectronic biosensor, photodetector, wireless.**

Manuscript received September 26, 2017; revised February 5, 2018; accepted March 4, 2018. This work was supported in part by the Natural Sciences and Engineering Research Council of Canada, in part by the Fonds de recherche Québec - Nature et technologies, and in part by the Microsystems Strategic Alliance of Québec. This paper was recommended by Associate Editor M. Kalofonou. *(Corresponding author: Benoit Gosselin.)*

M. N. Khiarak and B. Gosselin are with the Smart Biomedical Microsystems Laboratory, Université Laval, Québec, QC G1V 0A6, Canada (e-mail: mehdi.noormohammadi-khiarak.1@ulaval.ca; Benoit.Gosselin@gel.ulaval.ca).

E. Martianova, C. Bories, C. D. Proulx and Y. De Koninck are with the CERVO Brain Research Center, Université Laval, Quebec, QC G1J 2G3, Canada (e-mail: ekaterina.martianova.1@ulaval.ca; cyril.bories@gmail.com; Christophe.Proulx@fmed.ulaval.ca; Yves.DeKoninck@neuro.ulaval.ca).

S. Martel is with the NanoRobotics Laboratory, Montreal, QC H3C 3A7, Canada (e-mail: sylvain.martel@polymtl.ca).

Color versions of one or more of the figures in this paper are available online at http://ieeexplore.ieee.org.

Digital Object Identifier 10.1109/TBCAS.2018.2817200

I. Introduction

THE design of fluorescence biosensors have received lots of attentions, particularly in brain imaging, and in implantable fiber photometry applications for Ca^{2+} sensing [1]–[3]. In this scheme, dynamic fluctuations in calcium levels correlate with neural events, such as action potential generation, exocytosis of neurotransmitters, changes in synaptic plasticity, and gene transcription. Calcium transients, which are typically limited to slow variations, the bandwidth of which is of around 50 Hz [2], can be revealed in living animals by genetically encoded calcium indicators, such as GCaMP and RCaMP which are widely used in calcium fluorescence sensing and brain imaging, enabling the selective monitoring of neural activity of defined neurocircuits [2], [4]. However, the fluorescence signal power depends on several parameters, such as the type and intensity of light source excitation, which requires sensor interface circuits having a high dynamic range. Indeed, the fluorescence signal collected by a photodetector can range from a picoampere to a few nanoampere. Conventional apparatus for recording fluorescence signal typically consists of high-performance microscopy systems including different modules such as lasers, dichroic filters, photoreceivers, fiber-optic cannulas, fiber photometry consoles, etc., and using long tethered fibers to deliver light and to retrieve fluorescence signals [1], [5]. In [2], fiber photometry was used to study brain activity at the neural circuit level during social behavior in mice. They utilized bulk microscopy and a bench-top lock-in amplifier coupled to a femtowatt silicon photoreceiver to retrieve the fluorescence signal from the target tissue. Fiber optic based microprobes with tips $\leq$10 μm enabling optical detection of individual neurons deep in brain tissue have been designed and tested [1]. The fluorescence light is collected by a photomultiplier tube (PMT) detector, which is bulky and requires a high operating voltage ($\geq$100 V). Such experimental setups are reliable and precise, but also impractical for conducting long-term photometry experiments with live laboratory animals, due to the fiber/cable tethering and risk of breakage or injury. Fluorescence lifetime imaging microscopy (FLIM) systems contributed to simplify the bulky microscopy apparatus by replacing dichroic mirrors, emission filters, and excitation filters, in part, with highly sensitive integrated photodetectors and sensory circuits. In this scheme, a set of very short optic pulses (e.g., the pulse width is

1932-4545 © 2018 IEEE. Personal use is permitted, but republication/redistribution requires IEEE permission.
See http://www.ieee.org/publications_standards/publications/rights/index.html for more information.

This article has been accepted for inclusion in a future issue of this journal. Content is final as presented, with the exception of pagination.

typically equal to 100 ps) are generated by a high speed laser diode exciting target cells at a given repetition rate. The fluorescence signal emitted from the cells is detected by a high sensitivity single photon avalanche photodiode (SPAD). The time difference between the excitation pulses and the detected signals is recorded to obtain a histogram mapping of the fluorescence life time [6]–[8]. The main drawback of this approach is that it requires a very short pulsed laser diode dissipating high power, and making this approach very challenging for implantable/head mountable or system-on-chip (SoC) solutions.

Chronically implantable optoelectronic neural interfaces have been developed for deep brain fluorescence imaging [9], [10]. However, due to their large size and high power consumption, these implantable devices can cause tissue lesions at insertion or persistent irritation during or after implantation, and yield engineering challenges for thermal management, encapsulation, scalability interconnections, power delivery, and external control. In general, optoelectronic interfaces for fluorescence signal sensing based on microelectronic technology can be categorized into two distinct approaches including, charge accumulation [9], [11]–[13] and current mode [3], [14] circuits. In the charge accumulation scheme, the photo-generated charge is accumulated on a small integration capacitor. Then, the charge is converted to a voltage signal, and fed to the subsequent analog building blocks for further signal processing. A capacitive transimpedance amplifier (TIA) is often preferred to the conventional 3 T active pixel sensor (APS) structure due to its high charge-to-voltage conversion gain enabling higher sensitivity [15]. Indeed, this application can deal with weak illumination causing only small photogenerated charges in the photodiode, thereby inducing very small voltage across the photodiode due to the large photodiode parasitic capacitor C_{pd}, e.g., a photodiode the size of which is 91.4 μm $\times$ 123 μm can have a parasitic capacitance of several picofarads [16]. Therefore, this shortcoming makes the 3 T architecture less attractive for high-sensitivity applications. Besides, these approaches often necessitate the utilization of low-frequency noise cancellation building blocks and precise timings and control sequences making their circuitry relatively complex and power consuming [11]. In the current mode, the input photogenerated current is converted to a voltage signal by a TIA with a feedback resistor [3], the gain and noise performance of which depends on the feedback resistor as well as the photodiode parasitic capacitance. Thus, as the feedback resistor increases, gain grows and the input referred current noise decreases accordingly. However, implementing a very big resistor on chip to increase the gain is unpractical, because it would occupy too much silicon area, and limit the TIA bandwidth leading to high power consumption [3]. Furthermore, the large input parasitic capacitance at the input of the TIA amplifies its noise, which is deteriorating the front-end noise performance [13].

This work presents a new on-chip high-precision CMOS biophotometry sensor incorporated within a head mountable fiber photometry device including a wireless transceiver and a diffuse excitation light source for enabling chronic utilization with live laboratory mice. A new energy-efficient high-sensitivity fluorescence biosensor using a differential capacitive TIA (DCTIA)-based sensing front-end merged with a 2nd order continuous-time incremental $\Sigma\Delta$ modulator is presented. It offers a simplified implementation as well as a low-power architecture leveraging a hardware sharing strategy. Furthermore, the incremental 2nd order modulator offers a high dynamic range and allows for the utilization of simplified digital building blocks, like a ripple counter and an accumulator, for the decimation filter implementation. The proposed light weight wireless head mountable fiber photometry system addresses the shortcomings of bench top fiber photometry systems, including the risk of cable/fiber breakage and injury while enabling freely moving studies. The system is intended for Ca^{2+} fluorescence signal sensing in the brain of live laboratory animals. Hence limiting the excitation light to the least power enabling long term monitoring without photobleaching and phototoxicity which is requiring a very sensitive sensor working under very low excitation light. The paper is organized as follows. The proposed CMOS fluorescence biosensor operation principle, design methodology, and low-noise design approach are described in Section II. The CMOS chip implementation is discussed in Section III. Section IV presents the biosensor integration within the proposed wireless head mountable fiber photometry device. Experimental and measurement results are presented in Section V, both for the CMOS biosensor and the wireless prototype. Section VI concludes the paper.

II. Proposed System Architecture

A. System Overview

The block diagram of the proposed head-mountable optical neural interface for chronic brain fluorescence sensing is shown in Fig. 1. It provides a new CMOS fluorescence biosensor, optical signal conditioning, diffuse light excitation, and wireless data transmission. Such a device must be small and lightweight enough to be carried on the head of a laboratory mouse. The system functions are realized by a CMOS custom integrated circuit (IC) and by discrete off-the-shelf optoelectronic components and a CMOS custom integrated circuit (IC). The CMOS integrated circuit contains on-chip dummy and sensing photodiodes, a current-to-voltage converter, a CT $\Sigma\Delta$ modulator, LED driver circuit, and digital control building blocks. The photodiodes detects the emitted fluorescence light, and converts it to an electrical current. The current-to-voltage converter converts the photocurrent into a voltage which is subsequently handled in the following building blocks. The modulator quantizes the voltage signal and generates a pulsed width modulated signal representing the input signal. The LED driver powers up the blue LED and keeps its forward current stable. The second part includes an implantable optical fiber, a blue LED as a diffuse excitation light source, a low-power microcontroller, and a power management unit (PMU). This fiber photometry device allows for bidirectional light interaction with neurons (excitation/sensing) using a single implantable fiber, like conventional bulky microscopic systems. The different components (CMOS chip, a dichroic mirror, drum lenses, etc.) are held in place by the head mountable system housing. The whole system allows for collecting and digitizing the weak fluorescence signal the duration

This article has been accepted for inclusion in a future issue of this journal. Content is final as presented, with the exception of pagination.

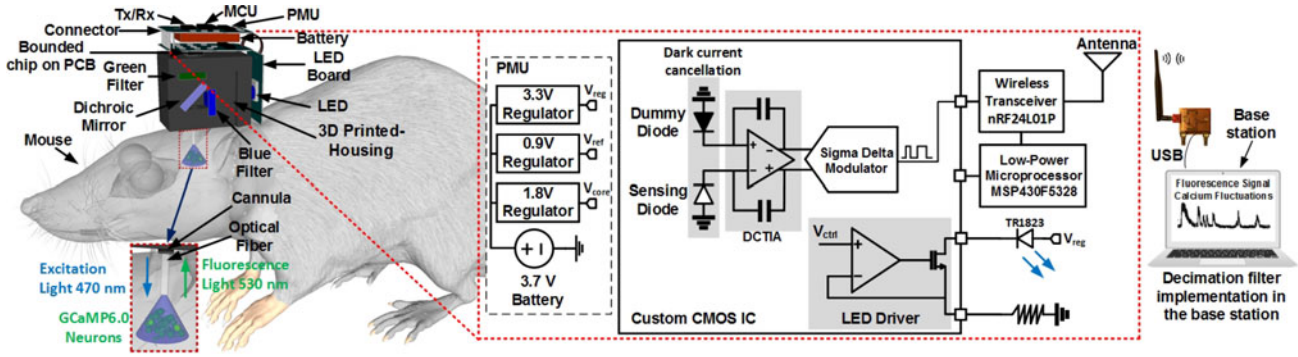

Fig. 1. Block diagram of the proposed optoelectronic neural interface. The system can excite a genetically encoded indicator like GCaMP6 expressed in neurons of a mouse's brain and record fluorescence signal through a single multimode optical fiber using the proposed custom integrated biosensor. The system transmits the neural data wirelessly to a base station connected to a computer host. The biosensor, the LEDs, the optical fiber, and the different optical components are enclosed within a lightweight wireless fiber photometry prototype that can be mounted on the head of a laboratory mouse for chronic utilization.

of which ranges from 30 to 50 ms [17]. A low-power microcontroller (MSP430F5328, Texas Instruments) provides the control signals for the wireless transceiver as well as the *clock* and the *reset* signals of the biosensor. The LED driver provides a maximum current of 200-mA to the LED with a forward voltage of 3.7 V in order to deliver sufficient optical power to the genetically modified neurons [18]. The PMU unit provides regulated supply voltages to all building blocks. The optical neural interface wirelessly transmits the fluorescence data collected by the CMOS biosensor to the base station through a low-power short range 2.4 GHz ISM data link.

B. Power Management Unit

The whole wireless biophotometry sensor interface is supplied by a 3.7-V, 100-mAh, 2.1-g Lithium-ion battery (Model 051417, MYD Technology). A low-dropout voltage, low-power (35 μA), and small size (1.5 $\times$ 1.5 mm^2) regulator (TLV70233, Texas Instruments) is used to provide a fixed 3.3-V for the transmitter, microcontroller, and the integrated CMOS chip electrostatic discharge (ESD) protection and guard rings. The PMU provides two stable 1.8-V (TPS72718DSET, Texas Instruments) and 0.9-V (TPS71709DSER, Texas Instruments) for the integrated biosensor chip. All of the regulator features a power supply rejection ratio (PSRR) more than 68 dB at 1 kHz to attenuate noise inductions especially into the biosensor chip from the optical stimulation circuity. The PMU unit use the small 1.5 mm $\times$ 1.5 mm 6-WSON package.

C. Wireless Transceiver

A low power single-chip wireless transceiver nRF24L01 from Nordic Semiconductor is utilized to transmit the recorded fluorescence data to a base station. The transceiver operates at a 2.4-GHz center frequency inside the industrial, scientific and medical (ISM) band. The transmitting mode of the transceiver draws a current of 11.3 mA from a supply voltage of 3-V at 0 dBm output power, while the receiving mode draws 12.3 mA. The maximum effective transmission rate of the transmitter is 1.4 Mbps which is sufficient to transmit the 20-kHz band limited output of the modulator to the base station. The transceiver is available in a small footprint 4 mm $\times$ 4 mm QFN20 package.

D. CMOS Custom Integrated Biosensor Design

Fluorescence biosensors based on charge accumulation, that typically include a photodetector, a DCTIA, a *correlated double sampling (CDS)* module, and an analog-to-digital converter (ADC), thus consisting of three individual cascaded building blocks to collect and convert the detected fluorescence signal into a digital bit stream [16]. In such systems, the fluorescence signal evoked by an external excitation light source is captured by a large differential femtowatt photodetector (i.e., 200 μm $\times$ 200 μm in this work) producing a photogenerated current that is converted into a voltage signal through the DCTIA. The latter building block is typically followed by a CDS block to suppress the $low\text{-}frequency\ noise$ and the $reset\ noise$, and by a data converter to generate a digitized output. More details on the operation of charge accumulation-based sensors are provided in [15]. Continuous-time sigma delta modulator (CTSDM) and data converters are well suited to interface with femtowatt photodetectors and DCTIA sensing modules as they can provide high precision and high dynamic range [11]. In this design, a DCTIA is used as the first stage integrator (Int_1) of a CTSDM modulator, thus fusing both building blocks together for increasing the hardware, noise and power efficiency by minimizing the number of cascaded blocks in the whole biosensor. Indeed, the DCTIA simultaneously acts as a pre-amplifier and a first integrator module of the $\Sigma\Delta$ modulator at once, which allows sharing the hardware to improve the energy efficiency and to simplify the whole sensor circuitry. This approach offers far greater benefits from power efficiency standpoint as the first integrator of the modulator topology is not traded-off for linearity, DC gain, and power consumption. The proposed fluorescence biosensor circuit schematic, including a sensing module (i.e., photodetectors) and a CTDSM associated with its timing diagram are depicted in Fig. 2. It comprises two photodiodes, a current buffer, a DCTIA, and a 2nd-order CT$\Sigma\Delta$ modulator. The parasitic input capacitors of the photodiodes are directly loading the input of the DCTIA. This large photodiode parasitic

This article has been accepted for inclusion in a future issue of this journal. Content is final as presented, with the exception of pagination.

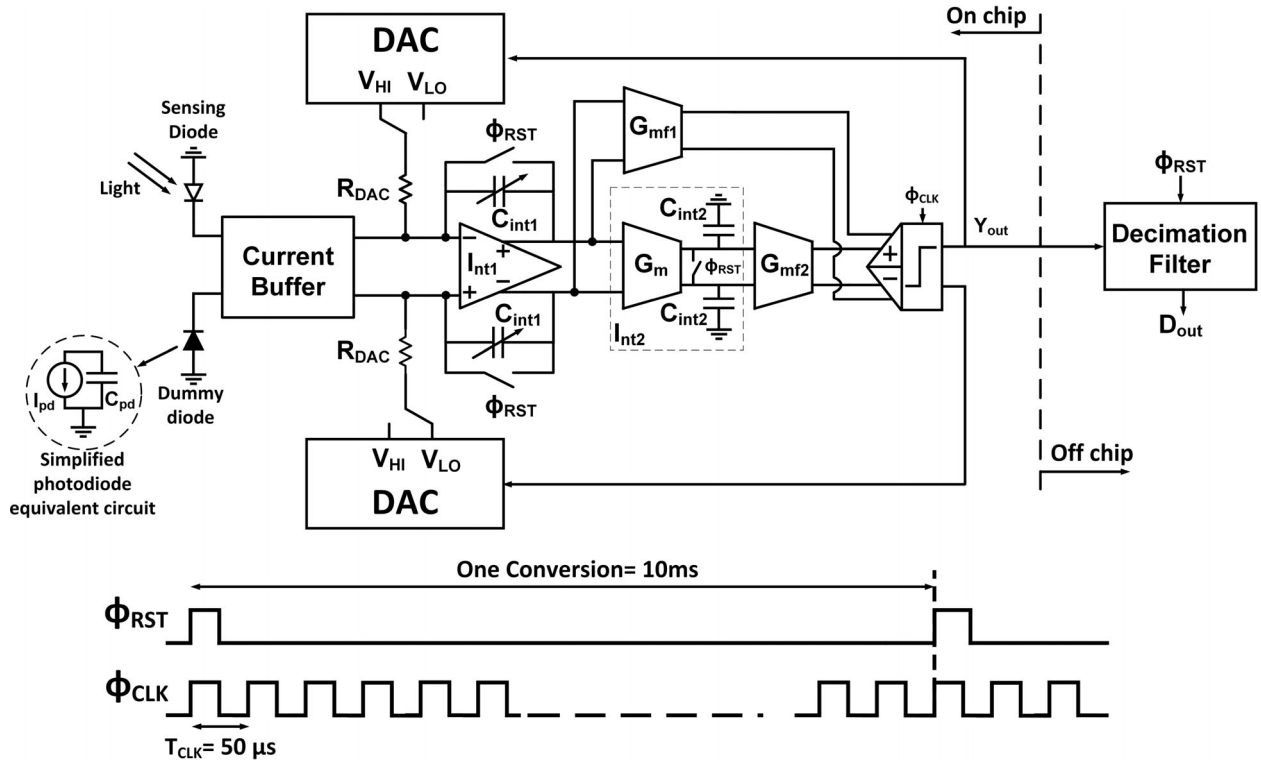

Fig. 2. Circuit schematic of the proposed high-sensitivity fluorescence biosensor including a DCTIA merged with a 2nd order CT $\Sigma\Delta$ modulator and its associated timing diagram. The DCTIA opamp DC gain is equal to 114 dB, $C_{\mathrm{int1}} = 100$ fF, $C_{\mathrm{int2}} = 400$ pF and R_{DAC} is equal to 10 MΩ.

capacitance can increase the noise in the DCTIA opamp [13]. Typically, a photodiode of this size in CMOS 0.18 μm has a parasitic capacitance of 5.7 pF, which is significant. Furthermore, this large parasitic capacitance can reduce the feedback factor of the CTIA through a capacitive divider $C_{\mathrm{int1}}/(C_{\mathrm{int1}} + C_{\mathrm{pd}} + C_p)$ where C_p is the opamp input node parasitic capacitance, that in turns can decrease the gain-bandwidth product (GBW), and increase non-linearity in the DCTIA. Hence, using a current buffer at the input of the DCTIA is essential to decouples the photodiodes parasitic capacitance from the DCTIA. The input photogenerated current I_{ph} is passed through the input current buffer and get integrated on the C_{int1} of the DCTIA input. As it can be seen, the core circuit is a CTSDM with two photodetectors as input signal sources. Thus, the effect of the dark current generated by the photodiode can be reduced by using a differential structure with a dummy photodiode [11]. While the sensing photodiode collects light generating both photocurrent and dark current, the dummy photodiode produces only dark current at its output. Consequently, dark currents of the two photodiodes acts as a common-mode signals and cancel out through the fully differential DCTIA. The simplified timing diagram, including the $clock$ and $reset$ pulse, is shown in Fig. 2. The operation of the biosensor begins with a global reset pulse that resets the voltage nodes and clears the memories in all analog and digital blocks. Note that the oversampling ratio (OSR) of the $\Sigma\Delta$ modulator is defined as the number of clock periods per conversion period (Fig. 2). Then, the modulator loop starts quantizing the input photogenerated current and generating the corresponding output bit stream. In this design, a 2nd order CTSDM allows

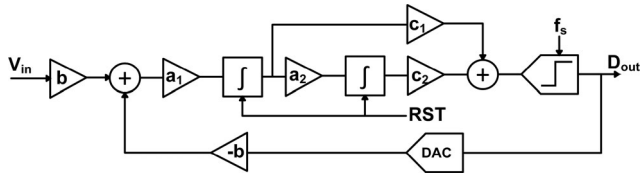

Fig. 3. Signal flow graph of the 2nd-order CT-$\Sigma\Delta$ modulator.

preventing idle tones in the output spectrum, whereas a single-bit quantizer enables for low distortion as it inherently has high linearity.

E. Design Methodology

This section explains the system-level design aspects of the continuous-time modulator including designing the noise transfer function (NTF), determining the loop filter transfer function, and optimizing the loop filter coefficients of the modulator. The block diagram of the proposed CT $\Sigma\Delta$ modulator is illustrated in Fig. 3. A cascade-of-integrators in feed-forward (CIFF) configuration is adopted to limit the swing in the integrators path and to minimize the performance degradation due to coefficient variations [19]. The adopted design methodology for the CT $\Sigma\Delta$ first consists of designing the discrete-time (DT) transfer function to meet the specifications, such as the desired SNDR, and then to obtain the continuous time equivalent transfer function through a DT-to-CT transformation. The desired DT $NTF(z)$ of the modulator is synthesized using the Schreier's Toolbox

This article has been accepted for inclusion in a future issue of this journal. Content is final as presented, with the exception of pagination.

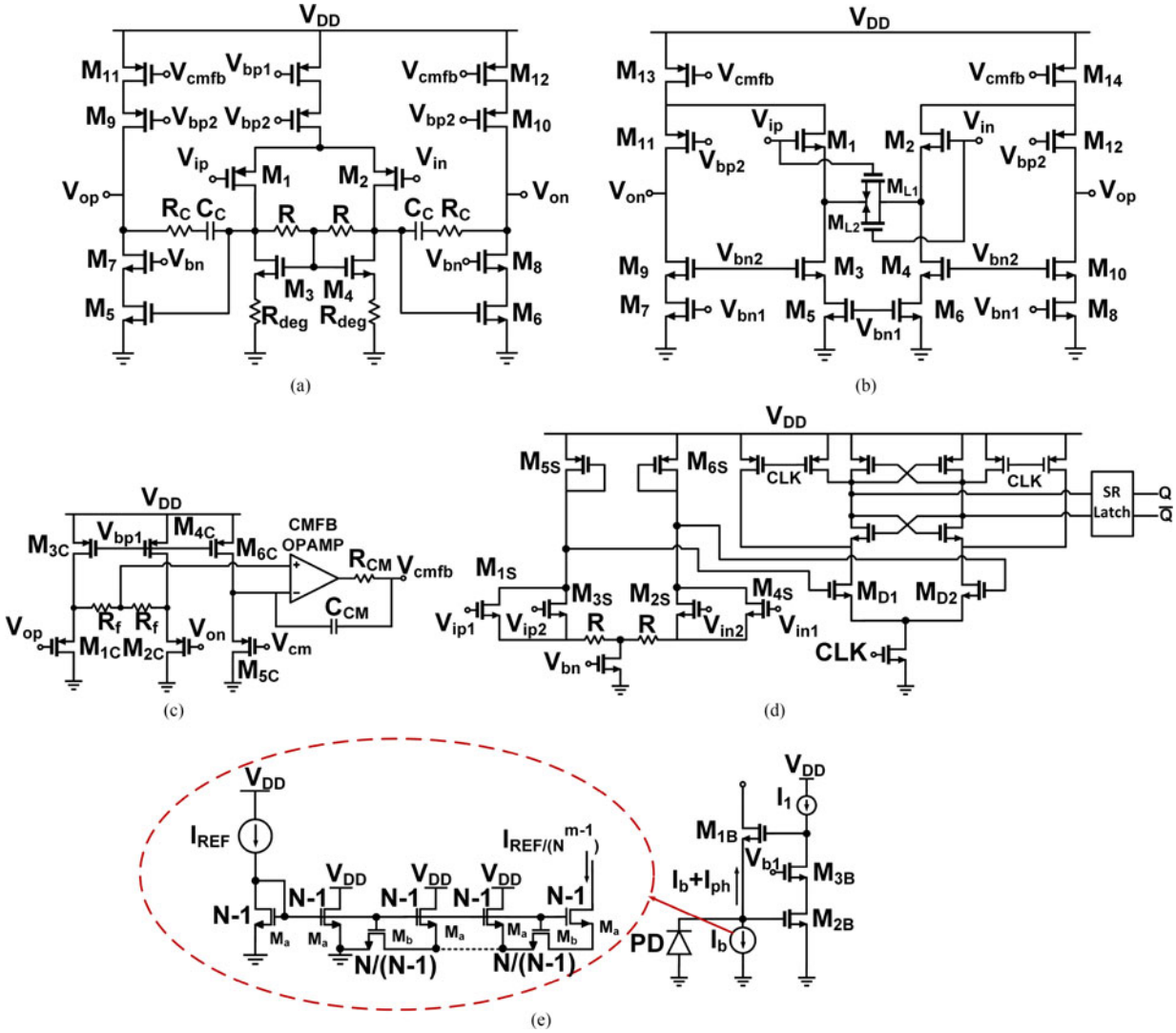

Fig. 4. Circuit schematic of (a) the low-noise two-stage opamp used in the Int_1, (b) the linearized folded cascode opamp used in the Int_2, (c) the common mode feedback circuit, (d) the feed-forward coefficient summation and quaitzer circuit, and (e) the input buffer associated with a current splitter.

[20], and gives

$$NTF\left(z\right)=\frac{1-2z^{-1}+z^{-2}}{1-0.9428z^{-1}+0.3333z^{-2}}. \tag{1}$$

The loop filter transfer function can be obtained by using $L(z)=1-1/NTF(z)$ given

$$L\left(z\right)=\frac{a_1b_1c_1-\left(a_1b_1c_1-a_1a_2b_1c_2\right)z^{-1}}{z^{-2}-2z^{-1}+1}. \tag{2}$$

Transient simulations are performed to assure that the integrators outputs are bounded to the full scale value. The resulting modulator's coefficient values, assuming a normalized sampling rate of 1, are summarized in Table I.

TABLE I
COEFFICIENT VALUES OF THE MODULATOR SHOWN IN FIG. 3

a_1	a_2	c_1	c_2	b
0.5	0.36	2	2	1

F. Low-Noise Circuit Design

In this section, the impact of the two main noise sources of the system, mainly the photodiode shot noise and the CMOS circuits noise (i.e., thermal and flicker noises), is analyzed. The shot noise can often be neglected at low illumination thanks to a small photogenerated current with respect to the circuit noise, while it can dominate at high illumination [21]. The DCTIA opamp introduces $1/f$ and thermal noises that should be taken into considerations, and by selecting a low-noise opamp topology, sizing large input transistors, using a circuit techniques to decrease the noise. Additionally, the reset switch injects kTC noise into the feedback capacitor; however, this noise only affects the initial state of the biosensor. Since it occurs only once at every conversion period, its effect is reduced by a factor equal to one OSR. Another important noise source is the noise from the feedback digital-to-analog converter (DAC) resistors that injects current thermal noise onto the C_{int1}. The power of this

This article has been accepted for inclusion in a future issue of this journal. Content is final as presented, with the exception of pagination.

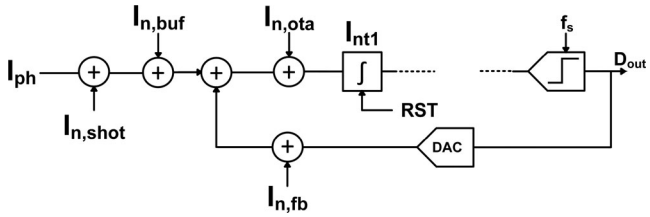

Fig. 5. Noise model of the CMOS sensor including all noise sources.

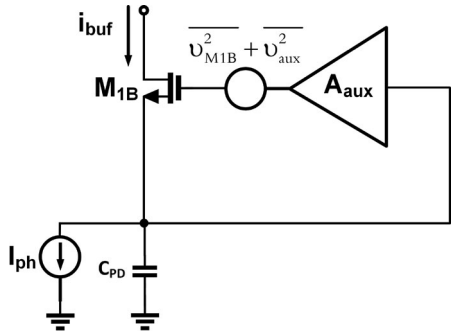

Fig. 6. Noise model of the input current buffer.

noise is inversely proportional to the resistor value, $R_{\rm DAC}$, that is designed to be large in this work. In [22], it was shown that the buffer reduces the DCTIA noise contribution and improves the entire system noise performance; however, it can introduce extra thermal noise. The dark current can be important in large photodiodes, thus limiting the sensitivity of the sensor. Hence, a fully differential structure can eliminate its effect at the cost of adding a dummy photodiode. The charge injection and clock feedthrough are also suppressed by the differential structure of the biosensor. Fig. 5 models the main noise sources that are located within the signal path to determine the input referred current noise. The shot noise originating from the photocurrent $i_{\rm ph}$ and the dark current $i_{\rm dc}$ are given by [23]

$$\frac{\overline{i^2_{n,\rm shot}}}{\Delta f} = q\left(i_{\rm ph} + i_{\rm dc}\right) \tag{3}$$

where q is the elementary charge of an electron, Δf is the single-sided bandwidth of the biosensor in Hz over which the noise is considered. The input current buffer introduces an extra noise which is mainly originating from transistor M_{1B} and the auxiliary amplifier, as shown in Fig. 6. The output current noise of the buffer can be expressed by

$$\frac{\overline{i^2_{n,\rm buf}}}{\Delta f} = \left(\overline{\upsilon^2_{M1B}} + \overline{\upsilon^2_{\rm aux}}\right)\left(\frac{g_{m,M1B}C_{PD}s}{C_{PD}s + g_{m,M1B}}\right)^2 \tag{4}$$

where $\overline{\upsilon^2_{M1B}}$ is the noise of M_{1B}, $\overline{\upsilon^2_{\rm aux}}$ is the auxiliary opamp output noise, $C_{\rm PD}$ is the photodiode parasitic capacitance, and $g_{m,M1B}$ is the transconductance of M_{1B}. The feedback DAC contributes to thermal noise through the resistor $R_{\rm DAC}$, which yields

$$\frac{\overline{i^2_{n,\rm fb}}_{n,\rm fb}}{\Delta f} = \frac{4kT}{R_{\rm DAC}} \tag{5}$$

where k is the Boltzmann's constant, T is the resistor absolute temperature, and $R_{\rm DAC}$ is the DAC rasistor. The first integrator ($I_{\rm int1}$) noise dominates the noise performance of the whole system (Figs. 5 and 2) by introducing flicker and thermal noise. Its contribution to the input-referred noise is given by

$$\frac{\overline{i^2_{n,\rm ota}}}{\Delta f} = \overline{\upsilon^2_{n,\rm ota}}\left(C_{\rm int1}s + \frac{1}{R_{\rm DAC}}\right)^2 \tag{6}$$

where $\upsilon_{n,\rm ota}$ is the Int1 opamp input referred noise and $C_{\rm int1}$ is the Int1 integration capacitor. The total input current noise density can be written as

$$\bar{i}^2_{n,\rm in} = \bar{i}^2_{n,\rm shot} + \bar{i}^2_{n,\rm buf} + \bar{i}^2_{n,\rm fb} + \bar{i}^2_{n,\rm ota} \tag{7}$$

The total RMS in-band noise at the input of the sensor can be calculated by integrating (7) over the passband f_B which is determined by the decimation filter cut off freqeuncy [24]. f_B is set according to the maximum input signal freqeuncy (i.e., maximum frequency of the fluorescence signal), which is 50 Hz.

$$\bar{i}^2_n = 2\int_0^{f_B}\left|\frac{\bar{i}^2_{n,\rm in}}{\Delta f}\right| df \tag{8}$$

$$\begin{aligned}\bar{i}^2_n = {} & \left(\bar{\upsilon}^2_{n,M_{1B}} + \bar{\upsilon}^2_{n,\rm aux}\right) g^2_{m,M_{1B}}\left(C_{\rm PD}f_B\right. \\ & \left. - g_{m,M_{1B}}\tan^{-1}\left(\frac{C_{\rm PD}f_B}{g_{m,M_{1B}}}\right)\right) \\ & + \frac{4KT}{R_{\rm DAC}}f_B + q\left(i_{\rm dc} + i_{\rm ph}\right)f_B \\ & + \bar{\upsilon}^2_{n,\rm ota}\left(C^2_{\rm int1}\frac{f^3_B}{3} + \frac{f_B}{R^2_{\rm DAC}}\right)\end{aligned} \tag{9}$$

The sum of all these noise sources contributions determines the noise floor. The measured input referred current noise is equal to 2.46 $pA_{\rm rms}$.

III. Circuit Design and Implementation

A. Loop filter

In this design, as mentioned earlier, a cascade-of-integrators in feed-forward (CIFF) configuration is adopted to limit the swing in the integrators path and to minimize the performance degradation due to coefficient variations. The Int_1 is the most critical analog building block of the whole $\Sigma\Delta$ modulator as any imperfections in this block can directly appear without suppression at the modulator output. Active RC-integrators are often employed for implementing highly-linear integrators compared to G_mC counterparts. Furthermore, as discussed earlier, the DCTIA operates as a charge-to-voltage converter merged with a first active integrator in the modulator loop. The DCTIA is realized by a feedback topology similar to an active RC-integrator in which a photocurrent integrator is realized by replacing the input resistance associated with an input voltage source with a photodiode as input current source. A two-stage fully differential amplifier topology with Miller capacitors frequency compensation and with nulling resistors is selected for the Int_1, as shown in Fig. 4(a). The opamp noise has a major impact on the noise performance of the sensor. In particular, the flicker noise ($1/f$),

This article has been accepted for inclusion in a future issue of this journal. Content is final as presented, with the exception of pagination.

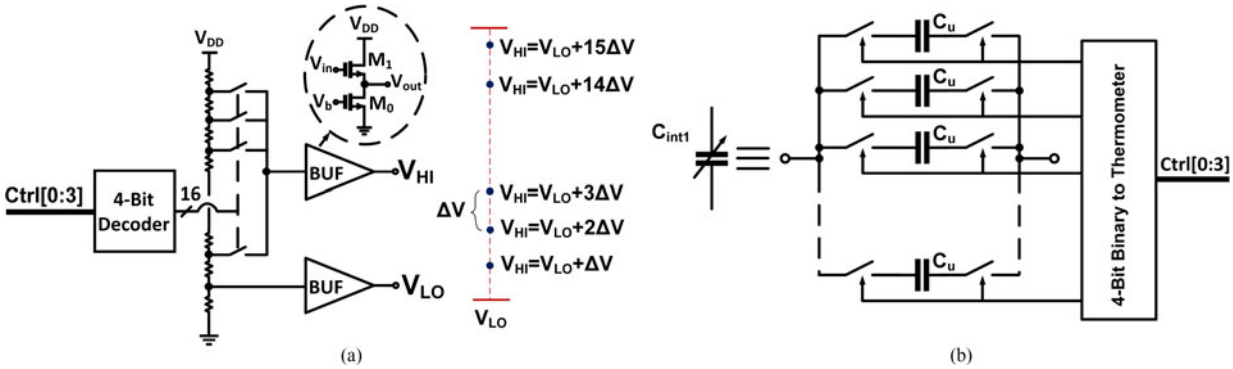

Fig. 7. (a) The schematic of the proposed DAC (b) tunable capacitor $C_{\mathrm{int}1}$ implementation.

is a major concern for a low-noise low-frequency circuits, thus pMOS transistors with large gate area ($W/L = 200\ \mu\mathrm{m}/2\ \mu\mathrm{m}$) are selected for the input transistors M_1 and M_2 to achieve low flicker noise and improve matching of the input differential pair. The flicker and the thermal noise contribution of M_3 and M_4 is minimized through the utilization of source degeneration resistors, R_{deg} with $g_{m\,3,4}R_{\mathrm{deg}} >> 1$ [24]. The noise contribution of the second stage of the opamp ($M_5 - M_{12}$) is divided by the first stage DC gain and its contribution can be neglected. The first stage common mode voltage is set by a simple local common-mode feedback (CMFB) circuit formed by R. Fig. 4(c) depicts the output stage CMFB which senses and stabilizes the output common mode voltage. The CMFB amplifier is realized through a single stage differential pair with active current mirror. The positive terminal of the CMFB amplifier senses a voltage approximately equal to $(V_{\mathrm{op}} + V_{\mathrm{on}})/2 + V_{\mathrm{SG},M1C}$, where $(V_{\mathrm{op}} + V_{\mathrm{on}})/2$ is the average output common mode voltage of the $Int1$, the value of which lies in the middle of the supply voltage ($V_{\mathrm{cm}} = V_{\mathrm{DD}}/2$). To compensate the effect of extra $V_{\mathrm{SG},M1c}$ voltage, a level shifter formed by M_{5C} and M_{6C} has been introduced between the V_{cm} and the positive terminal of the amplifier. The servo amplifier (CMFB opamp in Fig. 4(c) in the common mode circuit can introduce significant phase shift at high frequencies and yield instability in the common-mode loop. A crossover network formed by R_{cm} and C_{cm} is employed to detach the amplifier from the feedback loop at high frequencies and maintain the common mode stability [25]. The requirement on Int_2 including the output swing, GBW, slew rate, and DC gain are relaxed with respect to the first stage due to the noise-shaping characteristics of the loop filter. Fig. 4(b) illustrates the folded cascode structure implementing the second G_mC integrator. In addition, M_{L1} and M_{L2} at the sources of M_1, M_2 improve the linearity of the G_mC cell. The proposed feed-forward coefficient summation and the quantizer are depicted in Fig. 4(d). The summation block implements the weighted addition of the feedforward path coefficients of the $\Sigma\Delta$ modulator by converting the output of the integrators to weighted currents, by summing these currents, and by converting them back to a voltage signal at the quanitzer input [26]. A dynamic latched comparator, achieving low-power consumption by avoiding any static current consumption, is utilized to implement the quantizer. Large input devices M_{D1} and M_{D2} are used to minimize any input offset due to imperfections in the input differential pair. $\Sigma\Delta$ modulators achieve high resolution with relaxed matching requirements across their constitutive analog components thanks to *oversampling* and *noise shaping* in contrast with Nyquist rate ADCs. Furthermore, matching considerations have been taken into account in the sensor layout for minimizing performance degradation due to mismatch. The input current buffer, the DCTIA opamp, the second integration opamp, the summation block, the preamplifier, and the latch (Fig. 2) are laid out by interdigitating the transistors to meet the matching requirements. The common centroid method is used to lay out the resistors and the capacitors. The effects of transistors, capacitors, and resistors variation and mismatch effect on the SNDR are captured with Monte Carlo simulations and reported in Section V.

B. Feedback DAC

A conventional single-bit current DAC providing inherent linearity is employed in the modulator shown in Fig. 7(a). The DAC is a critical part of the proposed sensor, as it determines the quantization step size. It provides two reference voltages (V_{LO} and V_{HI}) can be asserted at the latch output. In the modulator, the difference between V_{LO} and V_{HI} defines the feedback coefficient as well as it determines the dynamic range of the modulator. The output voltage of the DAC is converted to a current through the resistor R_{DAC}, as shown in Fig. 2, which is subtracted from the input photocurrent. The resulting current difference is integrated on the $C_{\mathrm{int}1}$. In this design, the input photocurrent can range from a pA to a few nA. Thus, the DAC can be implemented using of a reference current source. However, current mode circuits are susceptible to channel length modulation, charge injection, and clock feedthrough [11]. More details about imperfections in current mode circuits for ADC can be found in [27]. Providing a small current in the order of nA from a DAC output, requires a large R_{DAC}, the size of which is often too big for an on chip implementation. To overcome this limitation, a small DAC reference voltage level (V_{HI}-V_{LO}) is chosen. This low reference voltage can be realized by a resistor divider, as shown in Fig. 7(a). However, to avoid the loading effect, a buffer is inserted between the resistor divider and the R_{DAC}. The buffer is implemented by a source follower made

This article has been accepted for inclusion in a future issue of this journal. Content is final as presented, with the exception of pagination.

of M_0 and M_1, which requires a minimum overdrive voltage across the current source M_0, for keeping the transistor in the saturation region. Thus, the minimum DAC reference voltage $V_{\rm LO}$ cannot be zero, and must be greater than the overdrive voltage of M_0. The minimum reference step size ΔV is designed to be 10 mV. The two DAC output reference voltage levels provide the required current for representing the different input light intensities. The maximum reference level is $V_{\rm HI}$-$V_{\rm LO}$ = 15ΔV, which determines the maximum non-saturation light intensity. The DAC reference level is controlled by the 4-bit decoder covering a variation range of 15-fold, extending the DR by 23.5 dB. It should be noted that, as the DAC reference level changes to set the required DR accordingly, a change in the modulator coefficient values of Int_1 can jeopardize the stability and performance of the loop. Thus, to avoid any instability, $C_{\rm int1}$ must be adjusted (Fig. 7(b)) according to the DAC reference level that is selected to cover a larger input light intensity. In this case, the feedback capacitor value is calibrated inserting unit capacitors in parallel with the $C_{\rm int1}$ through dedicated switches, as shown in Fig. 7(b).

C. Current Buffer

The input current buffer illustrated in Fig. 4(e) includes a regulated cascode nMOS transistor M_{1B} that is gain-boosted by M_{2B}, M_{3B}, and the current source I_1. The gain-boosting transistor M_{2B} keeps the voltage across the photodiode constant to increase the buffer linearity. A 500-pA DC current I_b is injected into the source of M_1 to improve the linearity performance at low $I_{\rm ph}$. The simulation reveals that the total harmonic distortion (THD) of the current buffer output $I_{\rm ph}$ is 110 dB. The implementation of the current source used to improve the linearity of the buffer is shown in inset in Fig. 4(e), and is similar to that reported in [28]. As seen in this Figure, the transistors are sized to ratios of either $W/L = N - 1$, $W/L = N/(N - 1)$, or $W/L = 1$, which allows to progressively divide the current by a factor of N to generate the desired current. In this case, the objective is to obtain a low current at only one of the output branches of the current source, while the rest of the output branches are connected to the supply voltage, providing a path for the currents.

D. Photodiodes

N-well/P-sub photodiodes with a size of 200 μm $\times$ 200 μm are used as dummy and sensing photodiode, respectively. These photodiodes benefit from a wider depletion region because they use low-doped n-well and a deeper n/p junctions thanks to a diffusion process that augments the collection efficiency of the junction. Moreover, this wider depletion region results in a smaller parasitic capacitance increasing the charge-to-voltage conversion ratio [15]. Both the photogenerated current and the dark current are proportional to the diode area [29]. Thus, bigger photodiodes can be used to increase the photon collection effect, while the dark current effect can be reduced by using two photodiodes (a photosensing and a dummy diode) and a fully differential circuit structures. Besides, instead of using a large photodiode, a small photodiode with an optical lens can be used

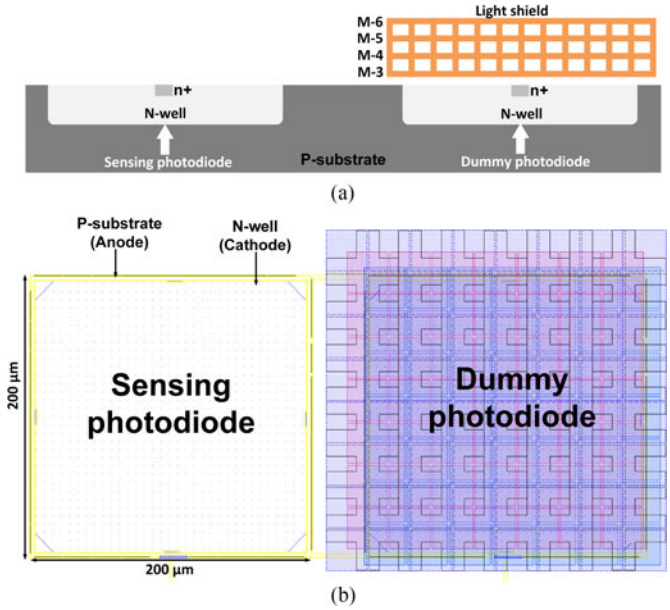

Fig. 8. (a) Cross-section of the photosensing and dummy photodiodes, (b) N-well/P-sub photosensing and dummy photodiode. The dummy photodiode is shielded using a high layer of interconnects (Metal 3- Metal 6) to block any spurious light other than the fluorescence signal from reaching the photosensing area.

to increase the photon collection effect, but the small size of the diode (e.g., 10 μm $\times$ 10 μm) renders the utilization of a lens difficult for this application. Both photodiodes, which are designed to occupy square areas, are closely located together in the chip layout to improve matching. The photodiodes are laid out close together with a p+ guard ring around the diodes where it is connected to the ground to absorb any induced noise and light diffusion to the dark photodiode. The photodiodes are not interdigitated because of the light leakage through the substrate on the dark photodiode. A small n+ well is used to connect the photodiode cathode node to the current buffer input. The diode is enclosed within P+ guard rings for grounding the substrate and for protecting the diode from substrate induced noise, digital spikes, supply noise. The layout of the photodiodes is shown in Fig. 8. The dummy photodiode is shielded using the high layer of interconnects (Metal 3- Metal 6) for blocking any spurious light from reaching the photosensing area of the dummy photodiode, as shown in Fig. 8. The corners of the photodiodes were cut to reduce their dark currents as suggested in [15].

E. LED Driver Circuit

Delivering light to a desired population of neurons can be accomplished through an implantable fiber using an embedded semiconductor light source, like a laser diode or a diffuse light-emitting diode (LED). Although they typically come with more coupling losses due to their diffuse light emission pattern, LEDs have several advantage over laser diodes such as lower cost, lower power and smaller size. LED have previously been used in calcium imaging experiments with freely moving laboratory animals [10]. Biophotometry applications

This article has been accepted for inclusion in a future issue of this journal. Content is final as presented, with the exception of pagination.

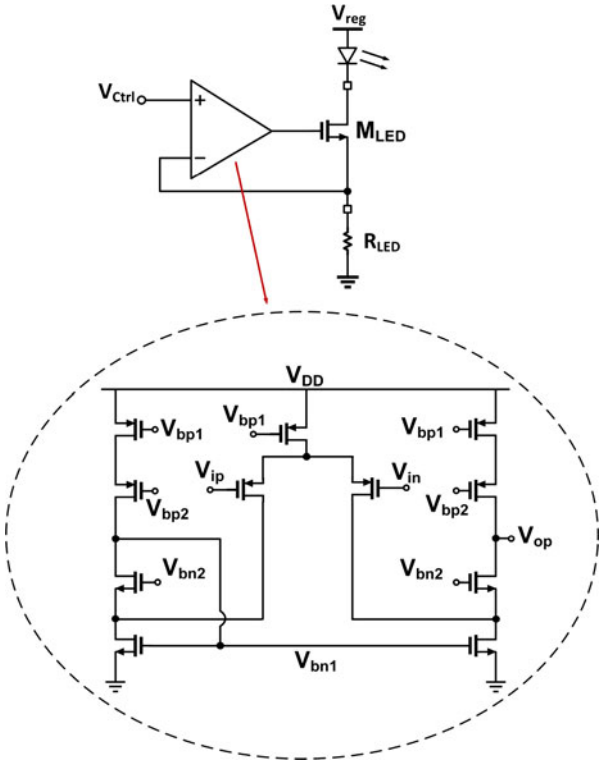

Fig. 9. Schematic of the LED driver circuit. The current flowing in the off-chip resistor R_{LED} is determined by V_{Ctrl} which is set off-chip with a resistor divider.

with genetically modified neurons typically require an excitation optical power of around 50 μW at the fiber tip [2], which requires that an appreciable amount of forward current passes through the LED, generating voltage drops as high as 3.3 V across the LED. Fig. 9 illustrates the schematic of the LED driver design used in the CMOS chip for providing a precise forward current through the LED. The amplitude of the current is determined by the off-chip voltage V_{Ctrl} and by the value of the off chip resistor R_{LED}. The LED driver circuit can power up an LED with a forward current as high as 200-mA. The maximum battery voltage allowed by a typical rechargeable Li-ion polymer battery is 3.7-V, for instance, whereas the typical LED forward voltage is below 3.3-V. In order to keep M_{LED} within the saturation region, the voltage drop across R_{LED} must be less than 200 mV in this design. Thus, a single-ended folded-cascode amplifier with input pMOS transistors (Fig. 9) is adopted to work with a low-input common mode voltage. This high gain (75 dB) amplifier lying in the negative feedback loop formed by M_{LED} keeps the voltage across R_{LED} equal to V_{Ctrl} regardless of the temperature and process variations.

F. Decimation Filter

The output PWM signal of the modulator Y_{out} is filtered with a digital matched filter to provide a digital output D_{out}. The transfer function of the matched filter is the exact replica of the analog loop filter transfer function given in (2). The matched filter, which is made of a cascade of digital integrators, is processing windows of $M = 200$ samples from the modulator all at once, for minimizing the number of modulator cycles required to achieve a given SNDR [30]. Parameter M represents the length of the finite impulse response (FIR) filter used for the matched filter, and equals the modulator OSR. This matched filter, which can be regarded as a M-length FIR filter with optimized coefficients [31], can be described by the difference equation $\omega(n) = \alpha_0 Y_{\mathrm{out}}(n) + \alpha_1 Y_{\mathrm{out}}(n-1) + \alpha_{N-1} Y_{\mathrm{out}}(n-N+1)$, where $\omega(n)$, $Y_{\mathrm{out}}(n)$, and $\alpha_0 ... \alpha_{N-1}$ are the input, the output, and the coefficients of the FIR filter, respectively. The coefficients can be optimized through the utilization of the built-in MATLAB optimization algorithm $fmincon$ [32], which searches to find a constrained minimum of a an objective function of multiple variables by starting from an initial estimate. The collected fluorescence signal that is converted to a PWM output signal by the proposed CMOS biosensor is transmitted to a base station using a commercial transceiver (nRF24L01P, Noridc Semiconductor). The digitized fluorescence signal is then retrieved after being decimated by the matched FIR filter implemented inside the base station, on the receiver side, in order to save significant power and area overhead on the head mountable system side.

IV. Wireless Fiber Photometry Prototype

One of the main challenges in fiber biophotometry consists of coupling the excitation light into a single fiber and receiving the fluorescence signal through this same fiber, without saturating the photodetector with the excitation light leakage. A solution to this problem consists of using different optical filters, including excitation and emission filters, to separate the excitation signal from the fluorescence signal. Additionally, a dichroic mirror is used to deflect off the blue light towards the implantable fiber (FT400UMT, ThorLabs) while transferring the fluorescence green light towards the CMOS detector. Two drum lenses are used as well to collimate the excitation light coming from the diffuse LED illumination source and the deflected fluorescence light coming out of the dichroic mirror, as shown in Fig. 10 [33]. The drum lenses (NT45-549, Edmund Optic, USA) used in the head mountable prototype are glass spheres, ground down axially to provide a mounting surface. These lenses are in fact used to improve the coupling between optical fiber and the light source and the CMOS sensor. The 3D representation of the prototype is shown in Fig. 10. The head mountable system plastic housing is realized with a 3D printer with Formlab's Black resin. A LED (LUXEON Rebel Blue SMD) controlled by the microprocessor and the integrated LED driver generates the blue diffuse excitation light. The blue light is passed through a drum lens located in front of the LED, and then through a dichroic mirror. The drum lens receives the diffuse blue excitation light and collimates it on the mirror for increasing the excitation light coupling efficiency into the fiber. The longpass mirror/beamsplitter spectrally separates excitation and fluorescence light by reflecting the light wavelength lower than the cutoff wavelength (e.g., 495 nm) and transmitting higher wavelengths. The excitation light ($\lambda = 470$ nm) is thereby deflected off through the mirror and directed to another drum lens located under the mirror, and ultimately, inside the fiber, as shown in Fig. 10. In this prototype, the fiber has a

This article has been accepted for inclusion in a future issue of this journal. Content is final as presented, with the exception of pagination.

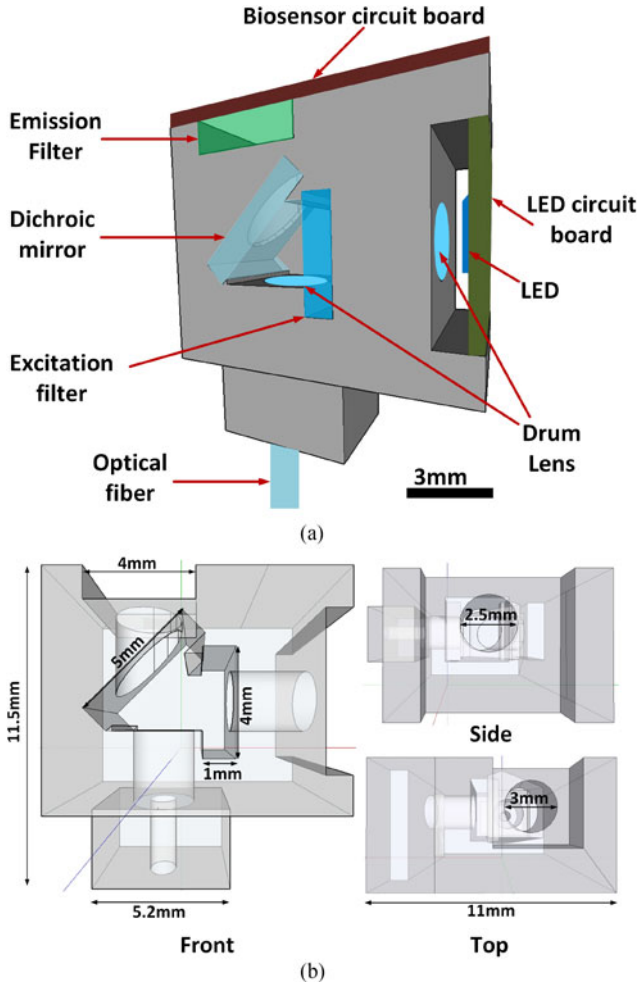

Fig. 10. The head mountable fiber photometry system. (a) Perspective view of all its components, (b) front, side, and top views of the plastic housing.

diameter of 400 μm while the mirror has a size of 4 mm $\times$ 5 mm $\times$ 1 mm. The drum lens allows to efficiently couple the blue light coming from the mirror into the fiber and vice versa. After the light goes through the drum lens and the fiber, it diffuses inside the tissues to reach the targeted cells. Then, the emitted fluorescence light returns through the same fiber, pass through the drum lens, through the mirror and through the green filter, towards the photosensor inside the CMOS chip. The longpass mirror is transparent to the fluorescence light (530 nm). Then, a green bandpass emission filter with a center wavelength of 530 nm further attenuates the excitation light leakage and blocks off any wavelengths other than the fluorescence light from hitting the photodetector. The emitted fluorescence light finally impinges on the on-chip photodetector. The characteristics of the optical components, including the filters, the lenses, the mirror, and the fiber used in the prototype are summarized in Table II.

TABLE II
FIBER PHOTOMETRY SYSTEM OPTICAL COMPONENTS

Parameters	Values
Excitation bandpass filter	470/24 nm (Chroma Technology)
Emission bandpass filter	535/50 nm (Chroma Technology)
Longpass dichroic mirror	495 nm (Chroma Technology)
Drum lens *	$EFL^{**} = 1.76$ mm (Edmund Optic)
LED	470 nm (LUXEON Rebel)
Optical fiber	Glass fiber with a diameter of 400 μm (ThorLabs)
System dimension (L $\times$ W $\times$ H)	11.0 $\times$ 6.0 $\times$ 11.5 mm^3

*Radius = 2.5 mm and Length = 3 mm **Effective Focal Lenght (EFL).

TABLE III
CHARACTERISTICS OF THE FIBER PHOTOMETRY SYSTEM

Parameters	Values
Brain interface	Single optical fiber
Dynamic range	86 dB
SNDR	70 dB
Sensitivity	24 mV/nW
Sampling rate	20 kSamples/s
Bandwidth	50 Hz
Minimum photodetection current	2.46 pA_{rms}
Transceiver center frequency	2.4 GHz
Optical fiber's diameter	400 μm
Dimensions (H $\times$ W $\times$ L, the optoelectronic interface w/o battery)	22 $\times$ 8 $\times$ 17 mm^3
Weight (the optoelectronic interface w/o battery)	3.6 g
Average LED power (1 LED, 580 mW @ 10%)	58 mW

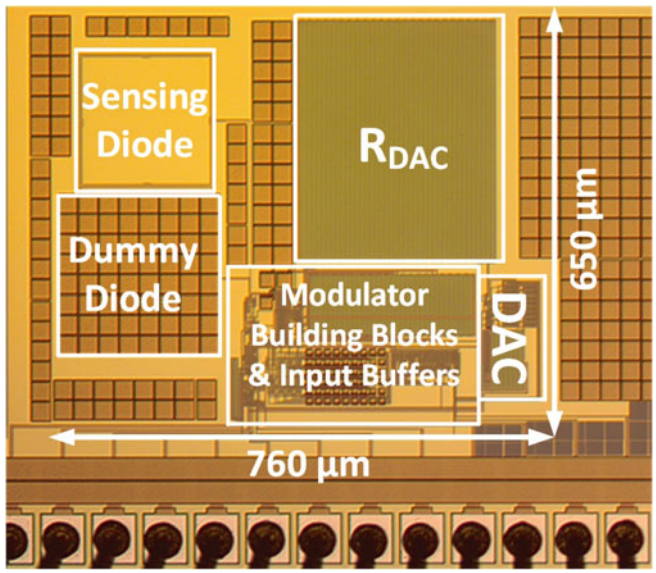

Fig. 11. Fabricated chip microphotograph in a 0.18-μm CMOS process with an area of 0.494 mm^2.

V. IMPLEMENTATION AND MEASUREMENT RESULTS

A. Chip Measurement

The proposed optoelectronic fluorescence biosensor is implemented in a 0.18-μm CMOS process. A chip microphotograph is depicted in Fig. 11. The chip active area excluding the bonding pads is approximately 0.494 mm^2. The dummy and photosensing photodiodes occupy 0.125 mm^2. The analog and digital modules of the biosensor are supplied by 1.8-V voltages. The CMOS chip and the microprocessor use separate grounds and decoupling capacitors that are placed between the analog and

This article has been accepted for inclusion in a future issue of this journal. Content is final as presented, with the exception of pagination.

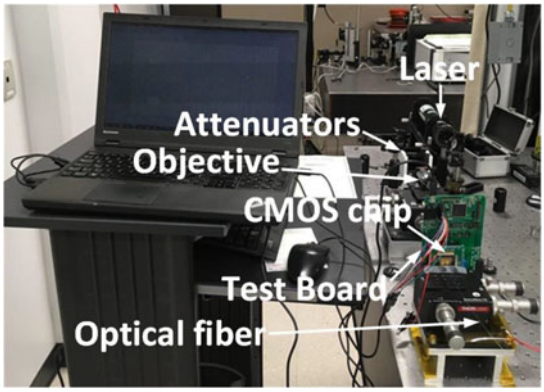

Fig. 12. Experimental setup for measuring the CMOS biophotometry sensor performance.

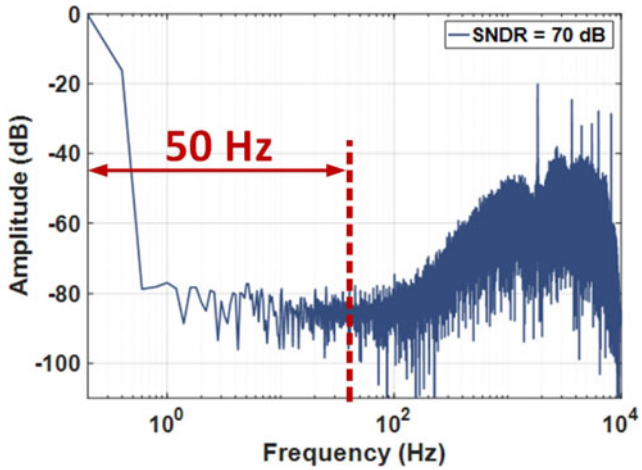

Fig. 13. Measurement results for the SNDR. A 100,000-points FFT is performed on the sensor output at a full scale input DC input light power.

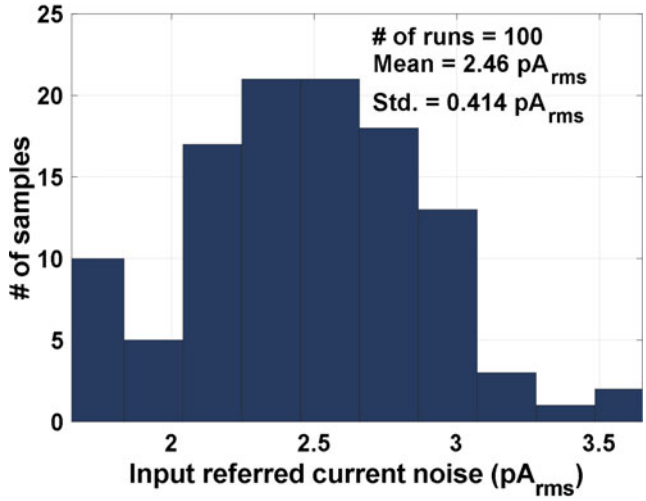

Fig. 14. Measured histogram for the sensor input referred current noise.

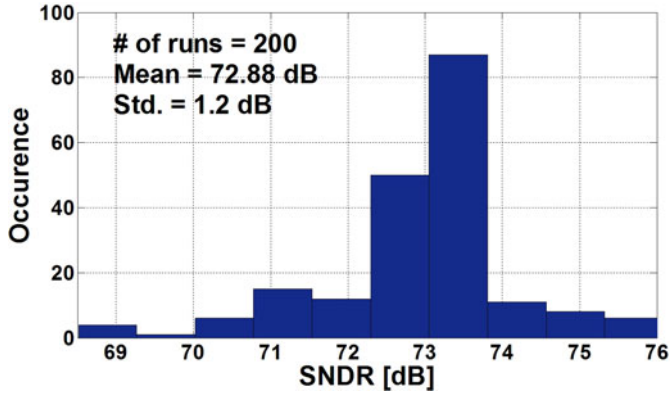

Fig. 15. Monte-Carlo simulation results for process variation and component mismatch of the presented biosensor.

the digital supply voltages and the ground connections to reduce noise. The total static power consumption of the sensor is 41 μW, where power consumption values of the Int_1 and Int_2 are each approximately equal to 14.4 μW. The experimental optical setup for evaluating the fabricated CMOS biosensor performance is depicted in Fig. 12. The light source consists of an Helium Neon (HeNe) laser at a wavelength of 633 nm and an output power of 4 mW, a polarizer to change the laser output power, mirrors, an objective lens, a fiber with a 225 μm core to provide input light to the CMOS photosensor. The chip is mounted on a test board connected to a Laptop computer to retrieve the measured data from the CMOS sensor. The output of the laser is aligned with the objective lens, and coupled to the fiber through the lens. Since the input photodiode area is 200 μm $\times$ 200 μm, the fiber allows to precisely couple the input light to the photosensor. The measured spectrum of the CMOS optoelectronic sensor at a full scale input light power is depicted in Fig. 13. The sampling frequency of the biosensor is 20 kS/s, and the peak SNDR is 70-dB for DAC values of 8 ΔV, over a 50 Hz signal bandwidth. The DR of the CMOS biosensor can be extended to 86 dB by digitally calibrating the modulator coefficients (i.e., by varying the effective value of $C_{\text{int}1}$), and by selecting a proper corresponding value for the DAC reference level. The readout noise comprises the photodiode shot noise and the circuit noise. Completely characterizing the noises effect at the output requires to measure the output for a full scale input incident power. Thus, the CMOS sensor is enclosed in a shielded box, isolated from EMI and any spurious light. Fig. 14 demonstrates a histogram of the input referred current noise of the fabricated sensor under such conditions [34]. Extensive simulation have been carried out to evaluate the implemented sensor over process and component variations. A histogram distribution obtained from a 200-run Monte-Carlo simulation is shown in Fig. 15. It demonstrates an average SNDR of 72.88 dB and a standard deviation of 1.2 dB indicating that even without coefficient tuning the SNDR performance is not significantly affected by the process and component variations. The decimation fitler output voltage versus the incident power at 633 nm is illustrated in Fig. 16. The measured sensitivity is approximately 24 mV/nW (incident optical power). The LED driver circuit consumes a power of 10 μW. Thanks to the proposed hardware sharing strategy and the merging of the modulator and the sensing block (DCTIA) together, operated from a 1.8-V power supply, the proposed sensor provides low power consumption

This article has been accepted for inclusion in a future issue of this journal. Content is final as presented, with the exception of pagination.

TABLE IV
PERFORMANCE SUMMARY AND COMPARISON WITH RECENT FLUORESCENCE BIOSENSORS

	[16]	[3]	[35]	[22]	[12]	[36]	[13]	This Work
Year	2017	2016	2017	2012	2016	2010	2017	2017
Data conversion	w/o ADC	w/o ADC	w/$\Sigma\Delta$ ADC	w/Two-step ADC	w/o ADC	w/o ADC	w/Two-step ADC	w/$\Sigma\Delta$ ADC
Process (μm)	0.065	0.18	0.25	0.35	0.35	0.18	0.18	0.18
Supply voltage	3.3 V	1.8 V	2.5 V	5 V	3.3 V	1.8 V	3.3 V	1.8 V
Sensing area (μm^2)	91.4 $\times$ 123	500 $\times$ 500	50 $\times$ 50	1390 $\times$ 1100	355 $\times$ 355	400 $\times$ 640	200 $\times$ 200	200 $\times$ 200
Sampling frequency (kS/s)	0.6667	1.024	10000	1.1	1	12–25	1	20
Minimum detectable current (fA_{rms})	0.33	–	10	6000	–	500 $\times$ 10^6	200	2460
Peak DR (dB)	94.8	80	116	101.6	61	75.56	94	86
Power consumption	66 mW	60 μW	118 mW	–	600 μW	12.97 μW	60 μW	41 μW

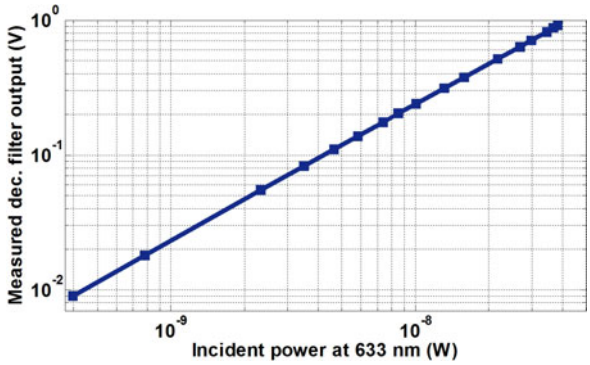

Fig. 16. Measured decimation filter output voltage with respect to the incident power at 633 nm.

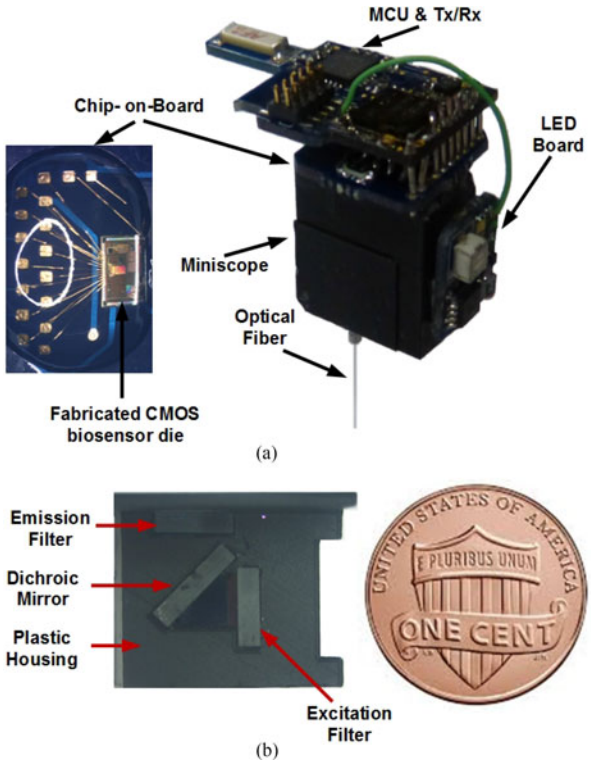

Fig. 17. (a) Miniature fiber biophotometry prototype including the fabricated CMOS sensor, a blue excitation LED, passive optical components, implantable fiber, plastic housing, etc. (b) side view of the wireless fiber photometry prototype plastic housing including the optical filters (emission and excitation filters) and the dichroic mirror.

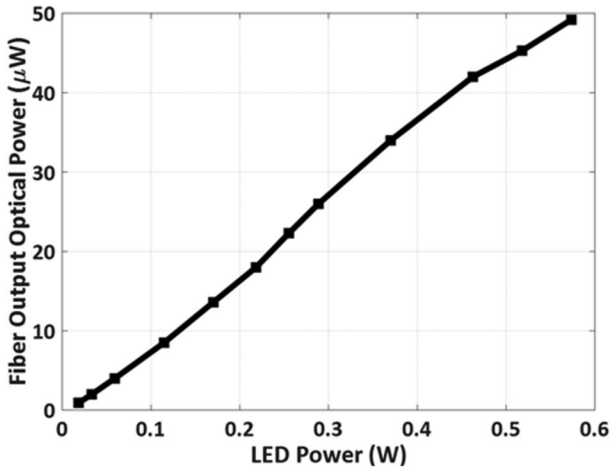

Fig. 18. Measured fiber output optical power versus LED power of the biophotometry system.

for similar precision and size, compared with recently reported sensors (Table IV).

B. Wireless Fiber Photometry System Performance

The 3D printed head mountable prototype with the filters, the lenses, the mirror, and the fiber is shown in Fig. 17. Rigid PCBs including the CMOS biosensor (photodetectors, the DC-TIA, the modulator, and the LED driver) and a few off-the-shelf electronic components are designed to fit on top and on the side of the plastic housing. All the optoelectronic components are mounted on the rigid PCBs including 3 rigid sections connected together through a custom designed rigid metal connectors to avoid using bulky board-to-board connectors. The miniaturized device results in a lightweight ($\leq$3.6 g, w/o battery) and compact device (22 $\times$ 8 $\times$ 17 mm^3). The whole fiber photometry system characteristics are summarized in Table III. The minimum fluorescence signal that can be detected depends on the sensor sensitivity, the coupling efficiency (numerical aperture of 0.39, etc.) of the fiber, and the losses in the optical path (i.e., fiber, lenses, dichroic filter, coupling, etc.) towards the photosensor. The minimum detectable incident optical power of the sensor is 9.6 pW. The measured excitation light source power versus the fiber output optical power is presented in Fig. 18. The output

This article has been accepted for inclusion in a future issue of this journal. Content is final as presented, with the exception of pagination.

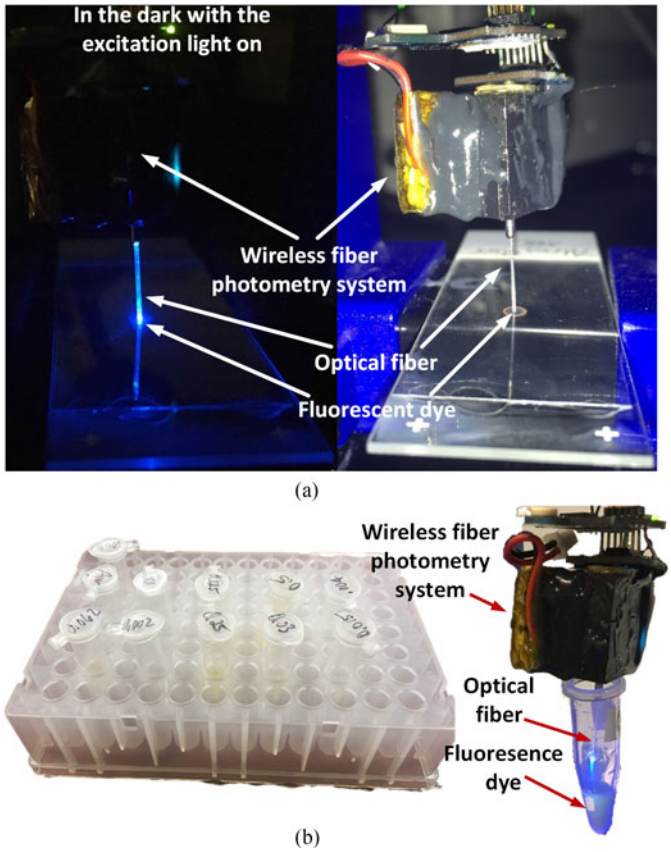

Fig. 19. (a) Fluorescence dye measurement experimental setup including the wireless fiber photometry system and Alexa fluor 488 (fluorescent dye) (b) different concentrations of fluorescence beads (FluoSpheres) in 0.5% AGAR to verify the performance of the proposed fiber photometry system.

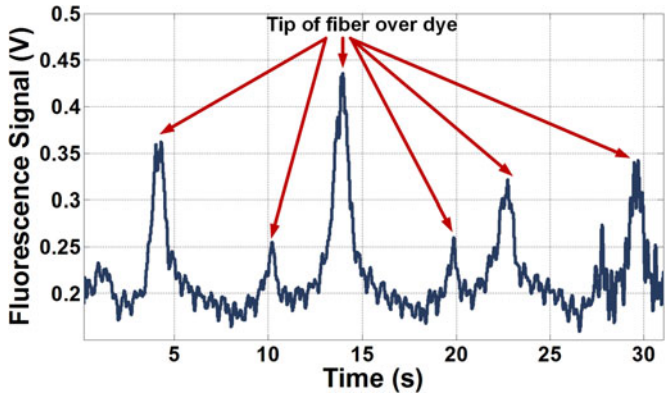

Fig. 20. Experimental results showing the measured fluorescence variation using an Alexa fluor 488 fluorescence dye in response to 30 μW excitation light while the tip of the fiber is passed repeatedly over the dye.

power of the fiber is estimated to 50 μW for a LED power of 580 mW.

C. Fluorescence Dye Measurement Results

2.5-μg of cholera toxin-subunit B conjugated with Alexa Fluor 488 is added on a glass slide (2–3 mm diameter). Alexa Fluor 488 is a green-fluorescent dye with excitation ideally suited to blue light. The fiber optic were lowered close to the dye by a holder. The experimental setup for fluorescence dye measurement is shown in Fig. 19(a). The recorded fluorescence data by the system is transmitted to a base station which is located 2 meters away. Fig. 20 illustrates the recorded fluorescence signal from Alexa flour 488 for an excitation light power of 30 μW when the fiber is passed over the dye repeatedly. Increasing concentration of FluoSpheres (0.001% to 0.125%) was embedded in 0.5% agarose gel. The tip of the fiber was placed immediately above the agarose-containing FluoSphere and fluorescence was measured using 50 μW excitation light. The recorded fluorescence signal versus different fluorescence beads concentrations is shown in Fig. 21.

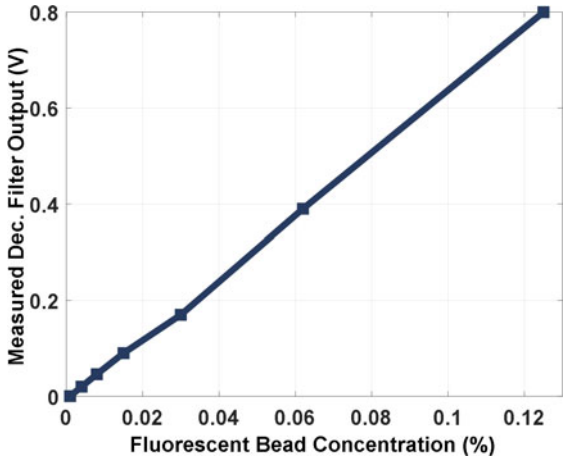

Fig. 21. Decimated output of the biosensor versus different fluorescence bead (FluoSpheres) concentrations in 0.5% AGAR.

VI. Conclusion

A CMOS optoelectronic fluorescence biosensor with embedded 2nd order $\Sigma\Delta$ modulation has been presented. A DCTIA structure allows canceling the differential dark current from on-chip dummy and sensing photodiodes both with sensing area of 200×200 μm^2. The proposed biosensor achieves a DR of 86 dB at a sampling frequency of 20 kS/s, sensitivity of 24 mV/nW, while significantly decreasing the power consumption down to 41 μW compared with previously reported biosensors. Additionally, the dynamic range of the biosensor can be further increased by controlling the DAC current amplitude in the $\Sigma\Delta$ feedback loop and by calibrating the modulator coefficients through a digitally programmable capacitor. A miniaturized head mountable system using the proposed CMOS biosensor is presented to conduct wireless brain biophotometry experiments with live laboratory mice. The device suppresses the excitation light leakage to the CMOS detector using a set of optical filters and a mirror, thus improving the system SNR compared to conventional approaches based on film filters. Therefore, the proposed CMOS optoelectronic biosensor is well suited for sensing weak input power fluorescence signal in low-power, small-size, high-precision miniature biophotometry applications, like for studying cell-type activity in small freely moving laboratory animals.

This article has been accepted for inclusion in a future issue of this journal. Content is final as presented, with the exception of pagination.

REFERENCES

[1] Y. LeChasseur *et al.*, "A microprobe for parallel optical and electrical recordings from single neurons in vivo," *Nature Methods*, vol. 8, pp. 319–325, 2011.

[2] L. A. Gunaydin *et al.*, "Natural neural projection dynamics underlying social behavior," *Cell*, vol. 157, pp. 1535–1551, 2014.

[3] M. N. Khiarak, B. Gosselin, S. Martel, and Y. De Koninck, "A CMOS lock-in-amplifier with semi-digital automatic phase tuning," in *Proc. IEEE Biomed. Circuits Syst. Conf.*, Oct. 2016, pp. 300–303.

[4] S. L. Resendez and G. D. Stuber, "In vivo calcium imaging to illuminate neurocircuit activity dynamics underlying naturalistic behavior," *Neuropsychopharmacology*, vol. 40, pp. 238–239, 2015.

[5] Doric Lens, 2017. [Online]. Available: http://doriclenses.com/

[6] M. Perenzoni, N. Massari, D. Perenzoni, L. Gasparini, and D. Stoppa, "A 160 × 120 pixel analog-counting single-photon imager with time-gating and self-referenced column-parallel A/D conversion for fluorescence lifetime imaging," *IEEE J. Solid-State Circuits*, vol. 51, no. 1, pp. 155–167, Jan. 2016.

[7] L. Pancheri, N. Massari, and D. Stoppa, "Spad image sensor with analog counting pixel for time-resolved fluorescence detection," *IEEE Trans. Electron Devices*, vol. 60, no. 10, pp. 3442–3449, Oct. 2013.

[8] Z. Li *et al.*, "A time-resolved CMOS image sensor with draining-only modulation pixels for fluorescence lifetime imaging," *IEEE Trans. Electron Devices*, vol. 59, no. 10, pp. 2715–2722, Oct. 2012.

[9] Y. Sawadsaringkarn, T. Miyatani, T. Noda, K. Sasagawa, T. Tokuda, and J. Ohta, "A CMOS optoelectronic neural interface device based on an image sensor with on-chip light stimulation and extracellular neural signal recording for optogenetics," *ITE Trans. Media Technol. Appl.*, vol. 1, no. 2, pp. 184–189, 2013.

[10] D. C. Ng *et al.*, "Real time in vivo imaging and measurement of serine protease activity in the mouse hippocampus using a dedicated complementary metal-oxide semiconductor imaging device," *J. Neuroscience Methods*, vol. 156, no. 12, pp. 23–30, 2006.

[11] M. N. Khiarak, S. Martel, Y. De Koninck, and B. Gosselin, "A high-sensitivity CMOS biophotometry sensor with embedded continuous-time sigma-delta modulation," in *Proc. IEEE Int. Symp. Circuits Syst.*, May 2017, pp. 1–4.

[12] X. Zhang, M. S. Noor, C. B. McCracken, Z. H. T. Kiss, O. Yadid-Pecht, and K. Murari, "CMOS image sensor and system for imaging hemodynamic changes in response to deep brain stimulation," *IEEE Trans. Biomed. Circuits Syst.*, vol. 10, no. 3, pp. 632–642, Jun. 2016.

[13] M. N. Khiarak *et al.*, "A high-precision CMOS biophotometry sensor with noise cancellation and two-step A/D conversion," in *Proc. 15th IEEE Int. New Circuits Syst. Conf.*, Jun. 2017, pp. 293–296.

[14] L. Yao, R. Khan, V. P. Chodavarapu, V. S. Tripathi, and F. V. Bright, "Sensitivity-enhanced CMOS phase luminometry system using xerogel-based sensors," *IEEE Trans. Biomed. Circuits Syst.*, vol. 3, no. 5, pp. 304–311, Oct. 2009.

[15] K. Murari, R. Etienne-Cummings, N. V. Thakor, and G. Cauwenberghs, "A CMOS in-pixel CTIA high-sensitivity fluorescence imager," *IEEE Trans. Biomed. Circuits Syst.*, vol. 5, no. 5, pp. 449–458, Oct. 2011.

[16] L. Hong, H. Li, H. Yang, and K. Sengupta, "Fully integrated fluorescence biosensors on-chip employing multi-functional nanoplasmonic optical structures in CMOS," *IEEE J. Solid-State Circuits*, vol. 52, no. 9, pp. 2388–2406, Sep. 2017.

[17] T. Chen *et al.*, "Ultrasensitive fluorescent proteins for imaging neuronal activity," *Nature*, vol. 499, pp. 295–300, 2013.

[18] G. Gagnon-Turcotte, Y. LeChasseur, C. Bories, Y. Messaddeq, Y. D. Koninck, and B. Gosselin, "A wireless headstage for combined optogenetics and multichannel electrophysiological recording," *IEEE Trans. Biomed. Circuits Syst.*, vol. 11, no. 1, pp. 1–14, Feb. 2017.

[19] J. Garcia, S. Rodriguez, and A. Rusu, "A low-power CT incremental 3rd order sigma delta ADC for biosensor applications," *IEEE Trans. Circuits Syst. I, Reg. Papers*, vol. 60, no. 1, pp. 25–36, Jan. 2013.

[20] R. Schreier, "The delta-sigma toolbox version 7.3," 2011. [Online]. Available: http://www.mathworks.se/matlabcentral/fileexchange/19-delta sigma-toolbox

[21] H. Tian, B. Fowler, and A. E. Gamal, "Analysis of temporal noise in CMOS photodiode active pixel sensor," *IEEE J. Solid-State Circuits*, vol. 36, no. 1, pp. 92–101, Jan. 2001.

[22] B. Liu and J. Yuan, "A quantum-limited highly linear monolithic CMOS detector for computed tomography," *IEEE Trans. Circuits Syst. I, Reg. Papers*, vol. 59, no. 3, pp. 566–574, Mar. 2012.

[23] H. Tian, B. Fowler, and A. E. Gamal, "Analysis of temporal noise in CMOS photodiode active pixel sensor," *IEEE J. Solid-State Circuits*, vol. 36, no. 1, pp. 92–101, Jan. 2001.

[24] T. C. Carusone, J. David, W. M. Kenneth, and D. Johns., *Analog Integrated Circuit Design*. Hoboken, NJ, USA: Wiley, 2012.

[25] S. Pavan and Y. Tsividis, *High Frequency Continuous Time Filters in Digital CMOS Processes*. Norwell, MA, USA: Kluwer, 2000.

[26] S. Pavan, N. Krishnapura, R. Pandarinathan, and P. Sankar, "A power optimized continuous-time sigma-delta ADC for audio applications," *IEEE J. Solid-State Circuits*, vol. 43, no. 2, pp. 351–360, Feb. 2008.

[27] J. Yuan, "Modeling, quantitative analysis, and design of switched-current pipeline A/D converters," *IEEE Trans. Circuits Syst. I, Reg. Papers*, vol. 56, no. 4, pp. 727–739, Apr. 2009.

[28] C. C. Enz and E. A. Vittoz, "CMOS low-power analog circuit design," in *Proc.Designing Low Power Digit. Syst., Emerg. Technol.*, 1996, pp. 79–133.

[29] S. Sze, *Physics of Semiconductor Devices*. Hoboken, NJ, USA: Wiley, 1981.

[30] Y. Chae *et al.*, "A 2.1 m pixels, 120 frame/s CMOS image sensor with column-parallel $deltasigma$ ADC architecture," *IEEE J. Solid-State Circuits*, vol. 46, no. 1, pp. 236–247, Jan. 2011.

[31] J. Markus, "High-order incremental delta-sigma analog-to-digital converters," Ph.D. thesis, Dept. Meas. Inf. Syst., Budapest Univ. of Technol. Econ., Budapest, Hungary, 2005.

[32] Mathworks, "MATLAB R2013a fmincon documentation," 2013. [Online]. Available: http://www.mathworks.com/help/optim/ug/fmincon.html

[33] W. A. L. III, L. N. Perkins, D. P. Leman, and T. J. Gardner, "An open source, wireless capable miniature microscope system," *J. Neural Eng.*, vol. 14, no. 4, 2017, Art no. 045001.

[34] A. Boukhayma, A. Peizerat, and C. Enz, "A sub-0.5 electron read noise VGA image sensor in a standard CMOS process," *IEEE J. Solid-State Circuits*, vol. 51, no. 9, pp. 2180–2191, Sep. 2016.

[35] A. Manickam *et al.*, "A fully integrated CMOS fluorescence biochip for DNA and RNA testing," *IEEE J. Solid-State Circuits*, vol. 52, no. 11, pp. 2857–2870, Nov. 2017.

[36] A. Hu and V. P. Chodavarapu, "CMOS optoelectronic lock-in amplifier with integrated phototransistor array," *IEEE Trans. Biomed. Circuits Syst.*, vol. 4, no. 5, pp. 274–280, Oct. 2010.

[37] K. K Ghosh *et al.*, "Miniaturized integration of a fluorescence microscope," *Nature*, vol. 8, pp. 871–878, 2011.

[38] C. K. Kim *et al.*, "Simultaneous fast measurement of circuit dynamics at multiple sites across the mammalian brain," *Nature Methods*, vol. 13, pp. 325–328, Feb. 2016.

Mehdi Noormohammadi Khiarak (S'15) was born in Azerbaycan, Iran. He received the B.S. degree in electrical engineering from Tabriz University, Tabriz, Iran, in 2009, and the M.S. degree in microelectronic circuits from the Sharif University of Technology, Tehran, Iran, 2012. He is currently working toward the Ph.D. degree at the Microelectronic Laboratory, Laval University, Quebec City, QC, Canada.

His main research interests include wireless implantable biomedical systems, optoelectronic neural interfaces, data converters, mixed-signal/analog IC design, and wireless data transmission.

Ekaterina Martianova received the B.Sc. and M.Sc. degrees in applied mathematics and physics from the Moscow Institute of Physics and Technology (State University), Moscow, Russia, in 2014 and 2016, respectively. She is currently working toward the Ph.D. degree in neurobiology at Laval University, Quebec, QC, Canada. Using fiber photometry calcium imaging in freely moving mice, her research interests include characterization of neuronal pathways important to guide normal behavioral response.

This article has been accepted for inclusion in a future issue of this journal. Content is final as presented, with the exception of pagination.

Cyril Bories received the Ph.D. degree in neuroscience from Université Laval, Quebec, QC, Canada, in 2013. He is currently an Associate Project Scientist with the Cervo Brain Research Centre, the Mental Health Institute of Quebec City, and the Canadian Brain Neurophotonic Platform, Quebec, QC, Canada. His current research interests include fundamental neuroscience to the development of new technologies to decipher the biological processes underlying neurological diseases with a special emphasis on aging, Alzheimer's disease, and chronic pain.

Sylvain Martel (F'15) received the Ph.D. degree in electrical engineering from the Institute of Biomedical Engineering, McGill University, Montreal, QC, Canada, in 1997. He is currently working toward the Postdoctoral degree at the Department of Mechanical Engineering, Massachusetts Institute of Technology, Cambridge, MA, USA, where he was appointed as a Research Scientist with the BioInstrumentation Laboratory. He is currently a Professor with the Department of Computer and Software Engineering, Institute of Biomedical Engineering, Polytechnique Montreal, Montreal, QC, Canada. He is a Fellow of the Canadian Academy of Engineering, the Chair of the IEEE Technical Committee on Micro-Nanorobotics and Automation, and the Director of the NanoRobotics Laboratory with Polytechnique Montreal. He was the recipient of many awards mostly in interdisciplinary research and is the Tier 1 Canada Research Chair in Medical Nanorobotics. He is currently leading an interdisciplinary team involved in the development of navigable therapeutic agents and interventional platforms for cancer therapy.

Christophe D. Proulx received the Ph.D. degree in pharmacology from Université de Sherbrooke, Sherbrooke, QC, Canada, in 2008. He was a Canadian Institutes of Health Research Postdoctoral Fellow in neurosciences with the University of California, San Diego, CA, USA. He is currently an Associate Professor with the Department of Psychiatry and Neurosciences, Université Laval, Quebec City, QC, Canada. He made significant contributions to understand synaptic dysfunctions underlying major depressive disorders. His research interests include fiber photometry calcium imaging, optogenetics, and electrophysiological recordings to study neural mechanisms of emotions. He is also interested to uncover cellular and synaptic mechanisms that can lead to mood disorders.

Yves De Koninck is currently a Professor of psychiatry & neuroscience with Laval University, Quebec city, QC, Canada, and is a world-expert in neurophysiology and optical technologies applied to neuroscience. He leads the Neurophotonics Center, Laval, QC, Cananda (www.neurophotonics.ca), where research in neuroscience drives the development of innovative new optical technologies. He was founding the Scientific Director of the Quebec Pain Network from 2002 to 2014 and the President of the Canadian Association for Neuroscience from 2010 to 2012. He is the Scientific Director of the Quebec Mental Health Institute and Member of the Centre d'Optique Photonique et Laser, Laval. He directs the CIHR Neurophysics Training Program Grant (www.neurophysics.ca). He served on multiple advisory and assessment committees for NSERC, CIHR, FRQS, NSF, NIH, the Wellcome Trust, and the French ANR. He made important contributions to understanding abnormal synaptic function underlying epilepsy, chronic pain, and aging-associated cognitive decline. In his laboratory, he discovered a novel mechanism underlying neuropathic pain involving chloride dysregulation responsible for spinal hyperexcitability, which led to four patents and the creation of a startup company for the development of novel analgesics. He is a Fellow of the Canadian Academy of Health Sciences and of the Royal Society of Canada. He was the 2013 recipient of the Jacques Rousseau Prize from Acfas for multidisciplinarity.

Benoit Gosselin (S'02–M'08) received the Ph.D. degree in electrical engineering from École Polytechnique de Montréal, Montreal, QC, Canada, in 2009, and he was an NSERC Postdoctoral Fellow with the Georgia Institute of Technology, Atlanta, GA, USA, in 2010. He is currently an Associate Professor with the Department of ECE, Université Laval, Quebec city, QC, Canada, where he is heading the Smart Biomedical Microsystems Laboratory. His research interests include wireless microsystems for brain computer interfaces, analog/mixed-mode and RF integrated circuits for neural engineering, interface circuits of implantable sensors/actuators, and point-of-care diagnostic microsystems for personalized healthcare. He is an Associate Editor for theIEEE TRANSACTIONS ON BIOMEDICAL CIRCUITS AND SYSTEMS and he is the Chair and the Founder of the Quebec IEEE CAS/EMB Chapter (2015 Best New Chapter Award). He served on the committees of several international conferences such as IEEE ISCAS, IEEE NEWCAS, BIOCAS, and IEEE EMBC/NER. His research interests include developing innovative microelectronic platforms to collect and study brain activity through advanced multimodal bioinstrumentation and actuation technology. In addition to earn several awards, such as the 2015 Mitacs Award for Outstanding Innovation and Best Paper Awards, his contributions led to the commercialization of the first wireless bioelectronic implant to combine optogenetics and large-scale brain monitoring capabilities within a single device, with his partner Doric Lenses, Inc.